

Four-channel CWDM device on a thin-film lithium niobate platform using an angled multimode interferometer structure

GENGXIN CHEN,¹ ZILIANG RUAN,¹ ZONG WANG,² PUCHENG HUANG,² CHANGJIAN GUO,^{2,3}  DAOXIN DAI,¹ KAIXUAN CHEN,^{2,3,4} AND LIU LIU^{1,*}

¹State Key Laboratory for Modern Optical Instrumentation, College of Optical Science and Engineering, International Research Center for Advanced Photonics, Zhejiang University, Hangzhou 310058, China

²Guangdong Provincial Key Laboratory of Optical Information Materials and Technology, South China Academy of Advanced Optoelectronics, South China Normal University, Higher-Education Mega-Center, Guangzhou 510006, China

³National Center for International Research on Green Optoelectronics, South China Normal University, Guangzhou 510006, China

⁴e-mail: chenkaixuan@m.scnu.edu.cn

*Corresponding author: liuliuopt@zju.edu.cn

Received 27 July 2021; revised 22 October 2021; accepted 25 October 2021; posted 28 October 2021 (Doc. ID 438816); published 9 December 2021

A compact and high-performance coarse wavelength-division multiplexing (CWDM) device is introduced with a footprint of 2.1 mm × 0.02 mm using an angled multimode interferometer structure based on a thin-film lithium niobate (TFLN) platform. The demonstrated device built on a 400 nm thick *x*-cut TFLN shows ultra-low insertion losses of <0.72 dB. Measured 3 dB bandwidths are 12.1 nm for all channels, and cross talks from adjacent channels are better than 18 dB. Its peak wavelength positions comply with the CWDM standard with a channel spacing of 20 nm. The filter bandwidth of the proposed CWDM device can be tuned by adjusting the structural parameters. This demonstrated CWDM device will promote future realization of multi-channel and multi-wavelength transmitter chips on TFLN. © 2021 Chinese Laser Press

<https://doi.org/10.1364/PRJ.438816>

1. INTRODUCTION

In the last decades, the photonic integrated circuit (PIC) has attracted much research interest, and enables integration of active and passive optical components on a single chip in a scalable manner. Numerous PIC platforms, such as silicon-on-insulator (SOI) [1], silicon nitride (SiN) [2], and indium phosphate (InP) [3], have been widely explored for photonic integration. Lithium niobate (LN), due to its wide transparent window, strong electro-optic (EO) effect, large nonlinear optical coefficient, and chemical stability, has been widely used in making various kinds of active optical components. Traditional waveguides on bulk LN are typically fabricated using technologies of titanium diffusion or proton exchange, which leads to an indistinct waveguide boundary and small index contrast between the waveguide core and its cladding regions [4]. Therefore, optical components fabricated on bulk LN are usually large, and high density integration is considered not feasible on this material platform. Recently, thin-film LN (TFLN) [5] has attracted a lot of attention due to its capability to support sub-micrometer-sized waveguides on LN, which can then lead to compact optical components as compared to those on bulk LN. Ultra-low-loss TFLN waveguides using a dry etching

technique [6] have already been demonstrated. Therefore, TFLN is considered as one of the most promising PIC platforms for future optical communications.

Due to the aforementioned large EO coefficient of LN, high-speed EO modulators on a TFLN platform, such as phase modulators [7], Mach-Zehnder modulators [8,9], Michelson interferometer modulators [10], and in-phase/quadrature modulators [11], have shown excellent performance as compared to their counterparts on other PIC platforms, such as SOI. As TFLN can simultaneously confine optical and acoustic modes, waveguide-based acousto-optic modulators working at sub-gigahertz acoustic frequencies have been demonstrated [12] based on suspended TFLN waveguides. Due to the large nonlinear optical coefficient and low linear waveguide losses, ultra-high-efficiency wavelength conversion with a normalized conversion efficiency of 4600%/(W · cm²) was achieved in a periodically poled TFLN waveguide [13].

Although a number of studies on active TFLN devices have been reported, there are still many passive devices worth exploring, such as wavelength-division multiplexing (WDM) devices. Combining WDM technology and high-performance EO modulators [14], multi-channel, multi-wavelength transmitter

chips, which are important components for data-center optical communications, can then be built on TFLN [15,16]. As LN is an anisotropic material, TFLN waveguides exhibit unique mode properties as compared to waveguides based on conventional isotropic materials [17]. It has been shown that significant polarization coupling related to mode hybridization through a waveguide bend can be observed. This has become the dominant factor limiting the compactness of on-chip routing for TFLN waveguides. Therefore, WDM devices using conventional structures such as array-waveguide gratings (AWGs) [18], planar concave gratings (PCGs) [19], and cascading Mach-Zehnder interferometers (CMZIs) [20] are difficult to design on the TFLN platform. Recently, a CWDM device using a multimode waveguide grating structure [21] on a hybrid platform consisting of TFLN and silicon rich nitride has been demonstrated at C-band. However, this structure is incompatible with state-of-the-art high-speed EO modulators on the monolithic TFLN platform discussed here. In this paper, we demonstrate a coarse WDM (CWDM) device based on an angled multimode interferometer (MMI) structure on the TFLN platform. The key part of the proposed device is essentially a straight multimode waveguide without involving any bending structures. Although CWDM devices using an angled MMI structure have been demonstrated on SOI and SiN platforms [22,23], implementations of such a structure, as well as efficient CWDM structures in general, on the TFLN platform are still missing. The proposed device here can support ultra-low insertion losses and cross talks for four supported wavelength channels, and can be adopted for CWDM transmitters at O-band.

2. DEVICE DESIGN AND PRINCIPLE

Figure 1(a) shows the schematic layout of the proposed four-channel CWDM device on TFLN. The basic structure consists of a multimode dispersive waveguide, i.e., the angled MMI of width W_{MMI} and lengths L_i ($i = 1, 2, 3, 4$) for the four output channels, and the corresponding input and output waveguides of width W_a and tilted angle θ with respect to the MMI structure. The input and output waveguides are all tapered to a relatively narrow width of W_{IO} to ensure single-mode input before entering the MMI. The transverse-electrical (TE) mode is considered throughout the structure. The input waveguide is put at the beginning of the MMI section, and the output waveguides are placed along the opposing edge of the MMI section according to the inverted self-imaging condition [22], as shown in Fig. 1(a). Due to the dispersion of the angled MMI section and the tilted input, the input signals are separated into different wavelength channels that are imaged at different axial positions L_i with respect to the input waveguide. The imaging length L_i can be defined using Eq. (1), which depends on the effective refractive index of the fundamental TE mode n_{eff} of the MMI section, the MMI width W_{MMI} , and the wavelength of the corresponding output channel λ_i :

$$L_i = \frac{4n_{eff}W_{MMI}^2}{\lambda_i}. \quad (1)$$

The channel spacing $\Delta\lambda$ of the adjacent channels for the proposed device can also be derived from Eq. (1) by taking a derivative with respect to λ on both sides, which gives

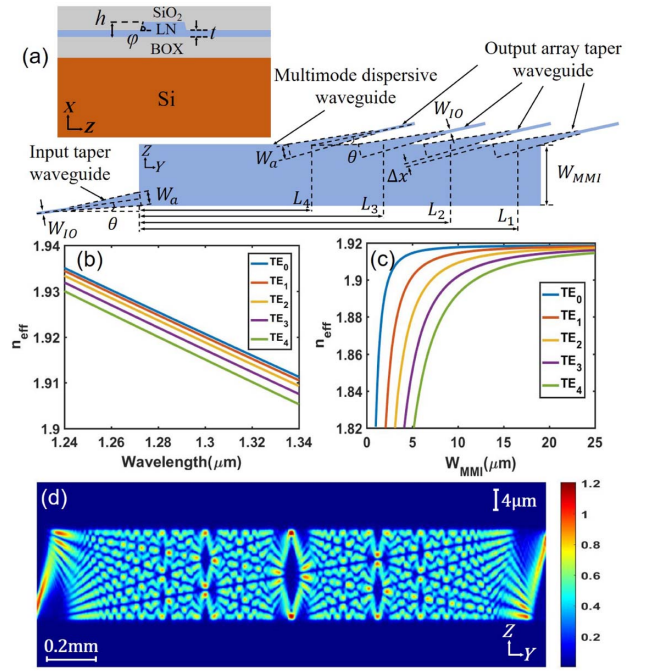


Fig. 1. (a) Schematic diagram of the four-channel CWDM on TFLN based on an angled MMI structure. (b) Calculated wavelength dependence of the n_{eff} curve for the first five TE modes at $W_{MMI} = 17.54$ μm. (c) Calculated n_{eff} curve of the first five TE modes at different W_{MMI} at a wavelength of 1300 nm. (d) Simulated light propagation in the proposed angled MMI structure.

$$|\Delta\lambda| = \frac{1}{4n_{eff}} \left(\frac{\lambda}{W_{MMI}} \right)^2 \frac{W_a + \Delta x}{\sin \theta}, \quad (2)$$

where Δx is the gap between the adjacent output waveguides and usually defines the resolution requirement of the proposed structure. Practically, Δx should be sufficiently large depending on the patterning tool used. In the proposed design, the whole structure is made on an x -cut TFLN layer, which is typically used for modulators and other devices on TFLN, with the optical axis, i.e., the z axis, of the LN material perpendicular to the MMI section as shown in Fig. 1(a). The thickness of the TFLN is 400 nm, and all the patterns shown in Fig. 1(a) are partially etched for 200 nm. The bottom and top cladding layers of the structure are all silicon oxide. Considering the wavelength channels (CWDM standard at O-band) and the resolution requirement for fabrication, we simulate the filter performance using a bidirectional eigenmode expansion (EME) algorithm (Lumerical MODE solution), and the structural parameters of the proposed device are carefully designed, and are summarized in Table 1. Figures 1(b) and 1(c) show the calculated

Table 1. Optimized Structural Parameters for the Four-Channel CWDM Device on TFLN

| $W_{MMI} = 17.54$ μm, $W_a = 5.54$ μm, $\theta = 0.17$ rad, $\Delta x = 0.88$ μm, $i = 1, 2, 3, 4$ | | | | |
|-------------------------------------------------------------------------------------------------------|------|------|------|------|
| Channel # | 1 | 2 | 3 | 4 |
| λ_i [nm] | 1271 | 1291 | 1311 | 1331 |
| L_i [μm] | 2054 | 2017 | 1980 | 1943 |

effective refractive index n_{eff} at different wavelengths and MMI widths for TE polarized modes. The MMI width W_{MMI} is first set to $17.54 \mu\text{m}$, which gives a reasonable overall length of the device around 2 mm , as well as low insertion losses. The light propagation in the MMI structure with a tilted input is shown in Fig. 1(d).

One can find that the minimal line width of the proposed design is $\Delta x = 0.88 \mu\text{m}$, which is within the resolution of typical patterning tools, such as a deep ultraviolet stepper or an electron beam lithographer (EBL). The input and output tapered waveguides have a length of $100 \mu\text{m}$, which are long enough and present negligible losses. Here, due to the non-vertical sidewalls resulting from LN etching (typically $\varphi = 60^\circ$), all the waveguide widths mentioned above refer to the top widths of the TFLN structures. The simulated wavelength responses of the four output channels in the optimized design are presented in Fig. 2(a). The resulting insertion losses for all four channels are $< 0.6 \text{ dB}$ at the corresponding CWDM channels with 3 dB bandwidths $BW_{3\text{dB}}$ of 12.4 nm .

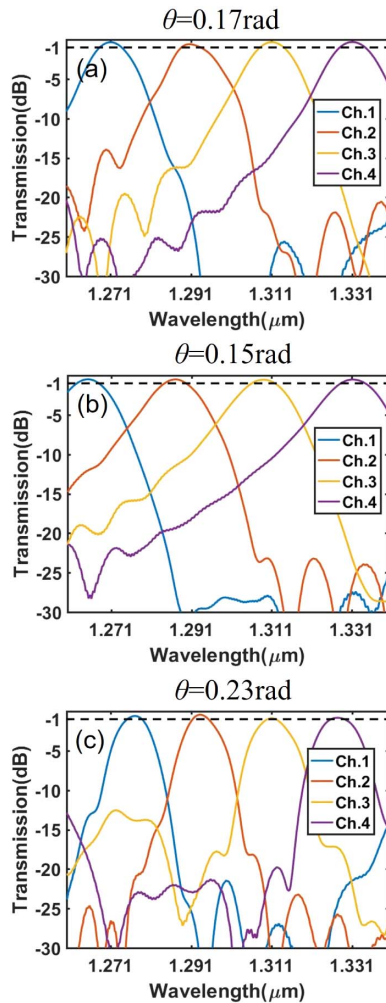


Fig. 2. Simulated spectral responses of the proposed CWDM device with different tilted angles: (a) $\theta = 0.17 \text{ rad}$, (b) $\theta = 0.15 \text{ rad}$, and (c) $\theta = 0.23 \text{ rad}$. The output waveguide spacing here is $\Delta x = 0.88 \mu\text{m}$.

To further investigate the flexibility of the proposed CWDM device, we analyze effects of the output waveguide spacing Δx and tilted angle θ on the transmissions. Figures 2(b) and 2(c) show the simulated spectral responses with different tilted angles ($\theta = 0.15 \text{ rad}$, 0.23 rad) but the same output waveguide spacing ($\Delta x = 0.88 \mu\text{m}$) with the structural parameters shown in Table 2. One can find that the 3 dB bandwidth of each channel can be tuned by changing the tilted angle θ . As θ increases, $BW_{3\text{dB}}$ decreases. For CWDM applications, the source wavelengths can vary for about 12 nm around the channel centers. This means that the tilted angle θ in the proposed structure should be sufficiently small so that the filter response can accommodate this wavelength variation. Further study suggests that θ should be smaller than 0.18 rad to keep the 3 dB bandwidth larger than 12 nm . Besides the bandwidth, the tilted angle θ also affects the peak wavelength positions. This is not desired for CWDM applications. Nevertheless, the output wavelengths can be aligned back at 1271 nm , 1291 nm , 1311 nm , and 1331 nm by adjusting the output waveguide positions, i.e., the waveguide spacing Δx . Figure 3 shows the corresponding re-aligned spectra for $\theta = 0.15 \text{ rad}$ and 0.23 rad with tuned structural parameters listed in Table 3. In these cases, Δx are $0.1 \mu\text{m}$ and $2.79 \mu\text{m}$,

Table 2. Structural Parameters of the Four-Channel CWDM Device on TFLN for Figs. 2(b) and 2(c)

| $W_{\text{MMI}} = 17.54 \mu\text{m}$, $W_a = 5.54 \mu\text{m}$, $i = 1, 2, 3, 4$ | | | | | |
|------------------------------------------------------------------------------------|-------------------------|------|------|------|------|
| Channel # | | 1 | 2 | 3 | 4 |
| $\theta = 0.15 \text{ rad}$ | λ_i [nm] | 1265 | 1287 | 1309 | 1331 |
| $\Delta x = 0.88 \mu\text{m}$ | L_i [μm] | 2064 | 2023 | 1982 | 1941 |
| $\theta = 0.23 \text{ rad}$ | λ_i [nm] | 1277 | 1292 | 1307 | 1322 |
| $\Delta x = 0.88 \mu\text{m}$ | L_i [μm] | 2041 | 2013 | 1985 | 1957 |

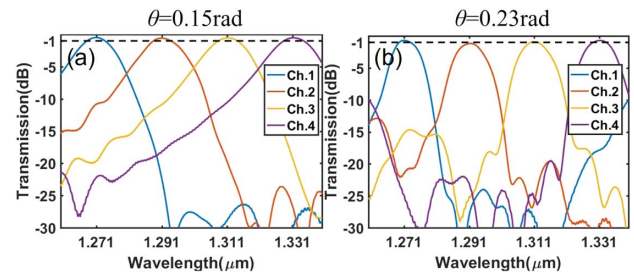


Fig. 3. Simulated spectral responses of the proposed CWDM device for (a) $\theta = 0.15 \text{ rad}$, $\Delta x = 0.1 \mu\text{m}$ and (b) $\theta = 0.23 \text{ rad}$, $\Delta x = 2.79 \mu\text{m}$.

Table 3. Structural Parameters of the Four-Channel CWDM Device on TFLN for Figs. 3(a) and 3(b)

| $W_{\text{MMI}} = 17.54 \mu\text{m}$, $W_a = 5.54 \mu\text{m}$, $i = 1, 2, 3, 4$ | | | | | |
|------------------------------------------------------------------------------------|-------------------------|------|------|------|------|
| Channel # | | 1 | 2 | 3 | 4 |
| $\theta = 0.15 \text{ rad}$ | λ_i [nm] | 1271 | 1291 | 1311 | 1331 |
| $\Delta x = 0.10 \mu\text{m}$ | L_i [μm] | 2053 | 2015 | 1977 | 1939 |
| $\theta = 0.23 \text{ rad}$ | λ_i [nm] | 1271 | 1291 | 1311 | 1331 |
| $\Delta x = 2.79 \mu\text{m}$ | L_i [μm] | 2053 | 2017 | 1981 | 1945 |

respectively, and $BW_{3\text{dB}}$ of channels are 14.8 nm and 10.4 nm, respectively. The above study indicates that the filter bandwidth of the proposed CWDM device can be designed according to requirements. It is also worthwhile to note that increasing θ also brings larger insertion losses as shown in Fig. 3. This is due to the fact that more high-order modes are excited at the MMI section when θ becomes larger. Some of the high-order modes are leaky due to the partially etched waveguide structure as mentioned before. These increased insertion losses at a larger θ can be suppressed, to some extent, by fully etching the TFLN.

The fabrication tolerance of the proposed CWDM device is also studied. The spectral responses of channel #1 with different L_1 , W_a , W_{MMI} , etching depth t , and total thickness of TFLN h are investigated. As shown in Fig. 4, the peak wavelength can be affected by variations of all the above structural parameters, but the spectral shape is barely changed. The sensitivity of the peak wavelength to changes in L_1 is only 0.5 pm/nm, while the variation in W_{MMI} results in a shift of the peak wavelength at a relatively large rate of 105 pm/nm. This is typical for an MMI structure. Variations in the widths of the input and output waveguides can also affect the peak wavelength position as shown in Figs. 4(c) and 4(d), but the effects are less than those induced by changes in W_{MMI} . Nevertheless, modern patterning tools, such as EBL, can ensure an accuracy of better than 10 nm, and therefore can support the fabrication of the proposed design. Moreover, tolerances to

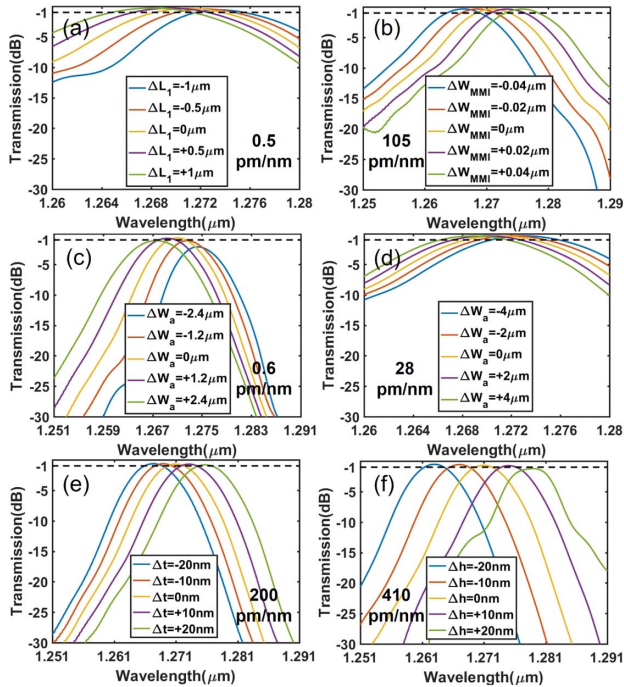


Fig. 4. Simulated fabrication tolerance of the proposed CWDM device with changes (a) in L_1 of ΔL_1 from -1 to $+1$ μm , (b) in W_{MMI} of ΔW_{MMI} from -0.04 to $+0.04$ μm , (c) only in input waveguide width W_a of ΔW_a from -2.4 to $+2.4$ μm , (d) in both input and output waveguide widths W_a of ΔW_a from -4 to $+4$ μm , (e) in t of Δt from -20 to $+20$ nm, and (f) in h of Δh from -20 to $+20$ nm for channel #1. Except for the one studied, the rest of the structural parameters are unchanged as shown in Table 1.

variations in the etching depth t and the total thickness of TFLN h also need to be considered. The peak wavelength shifts at a large rate of 200 pm/nm for variations in t as shown in Fig. 4(e). This effect can be released by tight control of the etching process using, e.g., an *in situ* film thickness measurement tool. Better than 5 nm etching depth accuracy can be achieved. As shown in Fig. 4(f), the sensitivity of peak wavelength to the total thickness is the largest (410 pm/nm) among all the structural parameters studied here. This indicates that the initial film thickness from the wafer vendor is critical for the proposed structure.

3. DEVICE FABRICATION AND MEASUREMENT

The designed angled MMI based four-channel CWDM device with parameters shown in Table 1 was then fabricated on a wafer (NanoLN) consisting of a 400 nm thick x -cut TFLN on a 3 μm buried SiO_2 layer. The structure was patterned using an EBL system (Raith 150 II), and a 200 nm thick LN layer was etched using inductively coupled plasma reactive ion etching technology. The device was then covered with an 800 nm thick SiO_2 layer deposited by plasma enhanced chemical vapor deposition. The 800 nm thick SiO_2 cladding layer was chosen here not only to protect the device, but also stay consistent with that used on an EO modulator on TFLN to achieve efficient

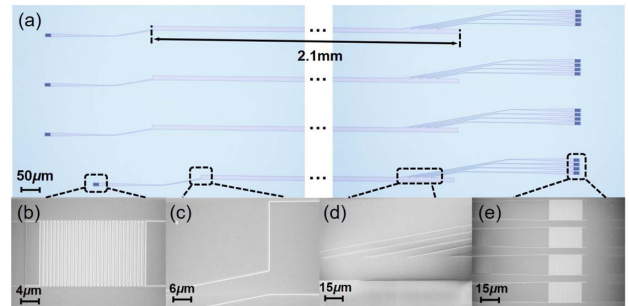


Fig. 5. (a) Microscope image of a fabricated device. Scanning electron microscope images of (b) input coupling grating, (c) input waveguide, (d) output waveguides, and (e) output coupling gratings.

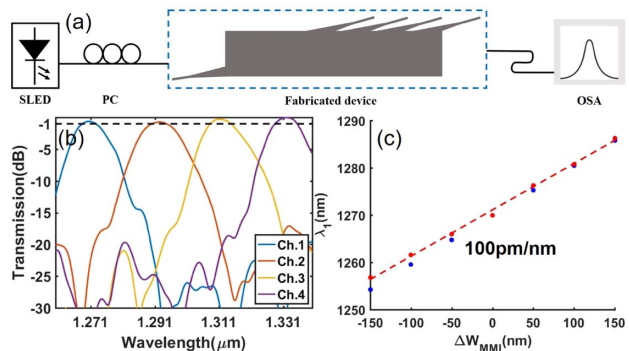


Fig. 6. (a) Schematic of the measurement setup. (b) Measured spectral response of the fabricated CWDM device. (c) Measured peak wavelength positions (red dots), linear fit (red dotted line), and simulated peak wavelength positions (blue dots) for channel #1 with variations in W_{MMI} .

Table 4. Performance Comparison of Different Types of CWDM Devices

| Device | Footprint (mm ²) | Channel Amount/Spacing (nm) | Insertion Loss (dB) | XT _{center} ^a (dB) | BW _{3dB} |
|----------------------------|------------------------------|-----------------------------|---------------------|----------------------------------------|-------------------|
| Si [19] PCG | 0.25 × 0.16 | 4/20.2 | 2.2 | 23.3 | NM ^b |
| Si [20] CMZI | 0.3 × 0.1 | 4/20 | ~1 | ~20 | 19 |
| Si [22] MMI | 0.012 × 1.21 | 4/21 | 2 | 20 | 12 |
| Si [25] MWG ^c | 0.6 × 0.04 | 4/20 | ~1 | ~20 | ~15 ^d |
| SiN [26] CMZI | 1 × 0.6 | 4/20 | ~1.8 | 15–24 | ~12 ^d |
| USRN [27] CVG ^e | 0.0006 × 8 ^f | 8/20 | 1 | 25 | 7.7 |
| SiN [23] MMI | 0.02 × 1.7 | 4/19 | 1.5 | 16–27 | 11 |
| SiN [21] MWG | 0.23 × 1.95 | 4/20 | <1.08 | 18 | 10 ^d |
| This work | 0.02 × 2.1 | 4/20 | <0.72 | ~18 | ~12.1 |

^aXT_{center} cross talks at central wavelength.

^bNM, not mentioned.

^cMWG, multimode waveguide grating.

^d1 dB bandwidth.

^eUSRN, ultra silicon rich nitride; CVG, coupled vertical grating.

^fThe footprint for each CWDM channel is 600 μm².

velocity matching [24]. Figure 5 shows some images of the fabricated device. The input and output TFLN waveguides are coupled to fibers using grating couplers (GCs) for measurement purposes.

The measurement setup is shown in Fig. 6(a). A broadband super-luminescence light emitting diode (SLED) at O-band (Thorlabs S5FC1021P) was used as the light source, and a polarization controller (PC) was used to align the input polarization to the TE mode. The output spectra were recorded using an optical spectrum analyzer (OSA, Ando AQ6317B). Figure 6(b) shows the measured spectral responses of the fabricated device. The responses of the GCs are normalized out by first measuring a reference structure consisting of two GCs and a short straight waveguide. For this chip, the fiber-to-grating coupling loss is about 3.56 dB per facet. It can be seen that the experimental results are in good agreement with the simulations. The insertion losses for the four channels are <0.72 dB with the best in channel #4. This is probably due to the fact that channel #4 is the first output channel, as shown in Fig. 1(a). The cross talks at the central wavelengths of all the channels are better than 18 dB. The reason that the measured cross talks are slightly better than the simulated ones is that in simulation, only one output channel is assumed. Practically, the measured cross talks may show better performances due to the fact that light from other channels is coupled out from the MMI structure. The 3 dB bandwidths are about 12.1 nm for all channels, which is consistent with the simulated results. In addition, Fig. 6(c) presents the peak wavelength positions of the measured spectra with respect to changes in the W_{MMI} . This reveals that the proposed device exhibits a linear sensitivity of about 100 pm/nm to ΔW_{MMI} , which also complies with the simulations. In Table 4, we summarize filter performances of the proposed device and those of similar CWDM devices on other platforms. One can find that the angled MMI based CWDM device shows similar performances on TFLN, SOI, and SiN platforms.

4. CONCLUSION

In conclusion, we have demonstrated a four-channel CWDM device on the TFLN platform using an angled MMI structure.

The key part of the proposed device is simply a straight multimode waveguide. This avoids using bent waveguides needed in other types of CWDM structures, whose radius is extraordinarily large in anisotropic planar structures such as TFLN [17]. The overall footprint of the proposed device is about 2.1 mm × 0.02 mm. Ultra-low insertion losses of <0.72 dB and averaged cross talks of 18 dB have been realized experimentally. As compared to the proposed device, the footprint of an MMI structure is much larger (15 mm) on the traditional bulk LN platform [28], and mode leakage losses will become obvious if the tilted angle is larger due to the low refractive index difference. This makes it hard to achieve an efficient CWDM device using the proposed structure based on traditional LN waveguides. We believe that further integration of the proposed device with high-speed EO modulators, and probably lasers [29], would lead to a fully integrated CWDM transmitter chip on TFLN.

Funding. National Major Research and Development Program (2019YFB1803902); National Natural Science Foundation of China (NSFC) (61961146003, 91950205); Guangdong Basic and Applied Basic Research Foundation (2021A1515012215); Science and Technology Planning Project of Guangdong Province (2019A050510039).

Disclosures. The authors declare no conflicts of interest.

Data Availability. Data underlying the results presented in this paper are not publicly available at this time but may be obtained from the authors upon reasonable request.

REFERENCES

1. B. Jalali and S. Fathpour, "Silicon photonics," *J. Lightwave Technol.* **24**, 4600–4615 (2006).
2. J. David, M. Roberto, L. Alexander, and L. Michal, "New CMOS-compatible platforms based on silicon nitride and Hydex for nonlinear optics," *Nat. Photonics* **7**, 597–607 (2013).
3. R. Nagarajan, M. Kato, D. Lambert, P. Evans, S. Corzine, V. Lal, J. Rahn, A. Nilsson, M. Fisher, M. Kuntz, J. Pluemeekers, A. Dentai, H. S. Tsai, D. Krause, H. Sun, K. Wu, M. Ziari, T. Butrie, M. Reffle, M. Mitchell, F. Kish, and D. Welch, "Terabits class InP photonic integrated circuits," *Semicond. Sci. Technol.* **27**, 094003 (2012).

4. Y. Qi and Y. Li, "Integrated lithium niobate photonics," *Nanophotonics* **9**, 1287–1320 (2020).
5. D. Zhu, L. Shao, M. Yu, R. Cheng, B. Desiatov, C. Xin, Y. Hu, J. Holzgrafe, S. Ghosh, A. Shams-Ansari, E. Puma, N. Sinclair, C. Reimer, M. Zhang, and M. Loncar, "Integrated photonics on thin-film lithium niobate," *Adv. Opt. Photon.* **13**, 242–352 (2021).
6. I. Krasnokutskaya, J. L. J. Tambsco, X. Li, and A. Peruzzo, "Ultra-low loss photonic circuits in lithium niobate on insulator," *Opt. Express* **26**, 897–904 (2018).
7. T. Ren, M. Zhang, C. Wang, L. Shao, C. Reimer, Y. Zhang, O. King, R. Esman, T. Cullen, and M. Loncar, "An integrated low-voltage broadband lithium niobate phase modulator," *IEEE Photon. Technol. Lett.* **31**, 889–892 (2019).
8. C. Wang, M. Zhang, X. Chen, M. Bertrand, A. Shams-Ansari, S. Chandrasekhar, P. Winzer, and M. Loncar, "Integrated lithium niobate electro-optic modulators operating at CMOS-compatible voltages," *Nature* **562**, 101–104 (2018).
9. M. He, M. Xu, Y. Ren, J. Jian, Z. Ruan, Y. Xu, S. Gao, S. Sun, X. Wen, L. Zhou, L. Liu, C. Guo, H. Chen, S. Yu, L. Liu, and X. Cai, "High-performance hybrid silicon and lithium niobate Mach-Zehnder modulators for 100 Gbit s⁻¹ and beyond," *Nat. Photonics* **13**, 359–364 (2019).
10. J. Jian, M. Xu, L. Liu, Y. Luo, J. Zhang, L. Liu, L. Zhou, H. Chen, S. Yu, and X. Cai, "High modulation efficiency lithium niobate Michelson interferometer modulator," *Opt. Express* **27**, 18731–18739 (2019).
11. M. Xu, M. He, H. Zhang, J. Jian, Y. Pan, X. Liu, L. Chen, X. Meng, H. Chen, Z. Li, X. Xiao, S. Yu, and X. Cai, "High-performance coherent optical modulators based on thin-film lithium niobate platform," *Nat. Commun.* **11**, 3911 (2020).
12. L. Shao, M. Yu, S. Maity, N. Sinclair, L. Zheng, C. Chia, A. Shams-Ansari, C. Wang, M. Zhang, K. Lai, and M. Loncar, "Microwave-to-optical conversion using lithium niobate thin-film acoustic resonators," *Optica* **6**, 1498–1505 (2019).
13. A. Rao, K. Adbelsalam, T. S. Aardema, A. Honardoost, G. F. Camacho-Gonzalez, and S. Fathpour, "Actively-monitored periodic-poling in thin-film lithium niobate photonic waveguides with ultrahigh nonlinear conversion efficiency of 4600% W⁻¹ cm⁻²," *Opt. Express* **27**, 25920–25930 (2019).
14. J. Cai, C. Guo, C. Lu, A. Lau, P. Chen, and L. Liu, "Design optimization of silicon and lithium niobate hybrid integrated traveling-wave Mach-Zehnder modulator," *IEEE Photon. J.* **13**, 2200206 (2021).
15. C. Zhang, S. Zhang, J. Peters, and J. Bowers, "8x8x40 Gbps fully integrated silicon photonic network on chip," *Optica* **3**, 785–786 (2016).
16. J. Hu, C. Li, C. Guo, C. Lu, A. Lau, P. Chen, and L. Liu, "Folded thin-film lithium niobate modulator based on a poled Mach-Zehnder interferometer structure," *Opt. Lett.* **46**, 2940–2943 (2021).
17. J. Wang, P. Chen, D. Dai, and L. Liu, "Polarization coupling of x-cut thin film lithium niobate based waveguides," *IEEE Photon. J.* **12**, 2200310 (2021).
18. P. Pan, J. An, Y. Wang, J. Zhang, and L. Wang, "Compact 4-channel AWGs for CWDM and LAN WDM in data center monolithic applications," *Opt. Laser Technol.* **75**, 177–181 (2015).
19. S. Pathak, P. Dumon, D. V. Thourhout, and W. Bogaerts, "Comparison of AWGs and Echelle gratings for wavelength division multiplexing on silicon-on-insulator," *IEEE Photon. J.* **6**, 4900109 (2014).
20. H. Xu and Y. Shi, "Flat-top CWDM (de)multiplexer based on MZI with bent directional couplers," *IEEE Photon. Technol. Lett.* **30**, 169–172 (2018).
21. Y. Liu, X. Huang, H. Guan, Z. Yu, Q. Wei, Z. Fan, W. Han, and Z. Li, "C-band four-channel CWDM (de)multiplexers on a thin film lithium niobate-silicon rich nitride hybrid platform," *Opt. Lett.* **46**, 4726–4729 (2021).
22. Y. Hu, R. Jenkins, F. Gardes, E. Finlayson, G. Mashanovich, and G. Reed, "Wavelength division (de)multiplexing based on dispersive self-imaging," *Opt. Lett.* **36**, 4488–4490 (2011).
23. T. Bucio, A. Khokhar, G. Mashanovich, and F. Gardes, "N-rich silicon nitride angled MMI for coarse wavelength division (de)multiplexing in the O-band," *Opt. Lett.* **43**, 1251–1254 (2018).
24. P. Kharel, C. Reimer, K. Luke, L. He, and M. Zhang, "Breaking voltage-bandwidth limits in integrated lithium niobate modulators using micro-structured electrodes," *Optica* **8**, 357–363 (2021).
25. D. Liu, M. Zhang, Y. Shi, and D. Dai, "Four-channel CWDM (de)multiplexers using cascaded multimode waveguide gratings," *IEEE Photon. Technol. Lett.* **32**, 192–195 (2020).
26. G. Gao, D. Chen, S. Tao, Y. Zhang, S. Zhu, X. Xiao, and J. Xia, "Silicon nitride O-band (de)multiplexers with low thermal sensitivity," *Opt. Express* **25**, 12260–12267 (2017).
27. G. F. R. Chen, J. W. Choi, E. Sahin, D. K. T. Ng, and D. T. H. Tan, "On-chip 1 by 8 coarse wavelength division multiplexer and multi-wavelength source on ultra-silicon-rich nitride," *Opt. Express* **27**, 23549–23557 (2019).
28. L. Shen, H. Wang, C. Xu, and W. Huang, "Numerical analysis of multimode interference effect in Ti:LiNbO₃ waveguides," *Proc. SPIE* **5970**, 59700W (2005).
29. Z. Ruan, Y. Zhu, P. Chen, Y. Shi, S. He, X. Cai, and L. Liu, "Efficient hybrid integration of long-wavelength VCSELs on silicon photonic circuits," *J. Lightwave Technol.* **38**, 5100–5106 (2020).